INTERNATIONAL JOURNAL FOR NUMERICAL METHODS IN FLUIDS, VOL. 14, 681–705 (1992)

NUMERICAL METHOD FOR UNSTEADY VISCOUS HYDRODYNAMICAL PROBLEM WITH FREE BOUNDARIES

PETER J. SHOPOV, PETER D. MINEV AND IVAN B. BAZHLEKOV

Center for Mathematics and Mechanics, Acad. G. Bontchev Str., bl. 8, PO Box 373, 1113 Sofia, Bulgaria

SUMMARY

A finite element method for the transient incompressible Navier–Stokes equations with the ability to handle multiple free boundaries is presented. Problems of liquid–liquid type are treated by solving two coupled Navier–Stokes problems for two separate phases. The possibility to solve problems of liquid–gas, liquid–liquid–gas or liquid–liquid–liquid type is demonstrated too. Surface tension effects are included at deformable interfaces.

The method is of Lagrangian type with mesh redefinition. A predictor–corrector scheme is used to compute the position of the deformable interface with automatic control of its accuracy and smoothness. The method is provided with an automatic choice of the time integration step and an optional spline filtration of the truncation error at the free surface. In order to show the accuracy of the method, tests and comparisons are presented. Numerical examples include motion of bubbles and multiple drops.

KEY WORDS Unsteady Navier–Stokes equations Finite element method Viscous flow Free boundary flow Multiphase flow

1. INTRODUCTION

Free surface problems for viscous incompressible flow occur often in nature and technology, e.g. extraction, sedimentation, capillarity, coating and polymer technology, biotechnology, chemical technology and so on. Usually, surface tension is presented at the fluid–fluid interface for immiscible media. Bubbles, drops, jets and films are classical examples of hydrodynamic objects with free surfaces whose transient behaviour and stability are important for technology. Objects composed of two liquids are of interest too: multiple drops, compound jets, compound films, etc.

A number of different numerical approaches have been developed for such problems based on relevant techniques for the fixed domain case.

The marker-and-cell (MAC) method of Harlow and Welch[1] and related finite difference methods in velocity–pressure variables (see e.g. References 2 and 3 and references cited therein) seem to be the first used for this class of problems. Such methods solve the transient Navier–Stokes equations in velocity–pressure variables. An example application of this method for a mechanical problem with a gas–liquid free surface—a splash of a liquid drop onto a plate or in a shallow or deep pool—is presented by Harlow and Shannon.[4] In this work the surface tension is not present at the interface but this restriction could be removed (see Reference 3 and references cited therein). Another important tool is the volume-of-fluid (VOF) method for the Navier–Stokes equations with free boundaries of Hirt and Nichols.[5] It also could include surface

0271–2091/92/060681–25$12.50

Received 8 May 1990
Revised 1 May 1991

tension. Although various problems have been solved by this technique, the surface tension approximation does not always work very well.[3]

Some ideas of Harlow and Welch[1] are used by Fromm[6] to develop a streamfunction method for liquid–gas deformable interface flows using a rectangular grid in the interior of the computational domain and special interpolation formulae near the free boundary. He has employed his method for solving a complicated problem of jet spreading from a nozzle driven by a pressure peak. This problem is related to jet printers. After a time period two changes of the computational domain geometry take place: initially the jet disintegrates into a drop and after that a small drop separates from the large one. In this problem the surface tension plays an essential role and it is important that during the simulation its approximation displays good properties.

A more precise description of surface tension seems to be achieved by a group of methods which employ a transform of the unknown domain to a standard one. Usually this approach is used for methods in streamfunction–vorticity variables, although it is obviously applicable also for velocity–pressure numerical methods. There are many works belonging to this class but we shall mention only a few of them. For example, a finite difference method for steady motion of an undeformable viscous drop in an unbounded liquid is presented by Rivkind *et al.*[7] and is generalized by Rivkind[8] for the case of a deformable drop. The numerical method of Ryskin and Leal[9,10] for steady motion of a deformable bubble is based on a similar idea. Another finite difference method for the same problem is developed and applied by Christov and Volkov.[11] The method of Ryskin and Leal[9] is generalized for transient deformation of a bubble in straining flow by Kang and Leal.[12] Another finite difference method for transient problems with a free surface of gas–liquid type is used to investigate jet stability by Shokoohi and Elrod.[13] The method of Ryskin and Leal[10] is extended for steady problems with one deformable liquid–liquid interface by Dandy and Leal,[14] who study the rise of a drop in an infinite liquid.

The velocity–pressure formulation seems to be more convenient than the streamfunction–vorticity one for the implementation of finite element methods in free surface viscous hydrodynamics. In this formulation the boundary conditions at the free surface are natural for the Navier–Stokes equations and are easily applied. Various numerical methods of finite element type are based on this approach in both Lagrangian and Eulerian reference frames.

A combination of the transformation to a standard domain and the MAC method in the context of finite elements is present by Piva *et al.*[15] It was successfully used for surface-tension-driven flows by Strani and Piva[16] and for thermocapillary convection by Strani *et al.*[17]

A general FEM scheme employing the Lagrangian approach is included in the book of Connor and Brebbia.[18] It uses ideas from the finite difference methods of Harlow and Welch[1] and Hirt *et al.*[2] In the Lagrangian approach the finite elements move with the liquid and after a certain time period they naturally become too distorted or stretched. Therefore a mesh redefinition has to be performed from time to time. A method of this type is used to model the behaviour of a bubble near a plate by Nakajima and Shima.[19] The free surface shape computed in this work is non-smooth and non-physical, which indicates poor approximation of the surface tension. Grid redefinition is not used and the calculations are simply stopped when the mesh becomes too irregular. An example of a fully developed finite element Lagrangian method is given by Bach and Villadsen[20] (see also references cited therein). They simulate a wave motion in a vertical film, employing a grid redefinition technique. Some comparisons of the numerical results with experiment are presented.

Finite element methods employing the Eulerian approach are widely used for stationary free surface problems. A review of such methods and the related references are presented in the book by Cuvelier *et al.*[21] One especially efficient method for such problems is proposed by Kruyt *et al.*[22] and a die-swell problem is treated numerically as an example.

The numerical methods for unsteady free surface viscous flow employing the Eulerian approach need an algorithm for finding the positions of the mesh nodes at each time level as a function of the position of the interface. The mesh nodes will not be fixed in time nor moving with the fluid as in the Lagrangian approach. This situation is considered by Lynch and Gray[23] for the flow in a deforming region and developed to the level of a general approach by Lynch.[24] No grid redefinition is required if the topology of the mesh is not changed during the calculations. A calculation of the element matrices is needed at every time step as for Lagrangian methods. A non-linear discrete system of equations is obtained for every time step owing to the presence of the classical convection matrix. The study of Keunings[25] is an example application of this approach to viscous free surface flows. The stability of Newtonian and viscoelastic jets is studied by direct simulation of the temporal development of the initial shape disturbance.

In the present paper a Lagrangian-type numerical method to handle the transient Navier–Stokes equations in velocity–pressure variables for domains with one or several free boundaries is presented. The surface tension is considered as an example of surface force. The method can treat one free boundary of the type gas–liquid and several of the type liquid–liquid. Its characteristic features are: automatic choice of the time integration step; automatic control of the accuracy of the computed free surface and its smoothness; optional usage of splines for the filtration of the error in the velocity at the interface; special procedure for solving the discrete system of equations and possibility to change the number of mesh nodes and mesh topology during the calculations.

The numerical method presented here is devised for numerical modelling of the transient behaviour of deformable fluid particles—bubbles, drops and multiple drops—but it could be applied to any other multiphase problems. Numerical examples involving flows of one, two and three liquid phases are considered.

Preliminary notes by Shopov[26] and Shopov *et al.*[27] contain information about this method. A numerical study of bubble motion to a rigid wall by Shopov *et al.*[28] is performed by means of the present method and contains a number of comparisons with the numerical and experimental results and asymptotic solutions of other authors. In this paper we concentrate our attention mainly on the description of the numerical method and present a couple of numerical examples in order to give a feeling for the scope of its possible applications.

The rest of the paper is organized as follows. The mathematical model to be considered is given in Section 2. In Section 3 the numerical method is described, while in Section 4 numerical examples are presented. Section 5 contains conclusions from the study.

2. GOVERNING EQUATIONS

Consider two immiscible liquids with deformable interfaces between them. We shall suppose that the sth liquid has constant density ρ_s and viscosity μ_s. The gas phase, if present, is assumed to be in contact with the first liquid (see Figure 1). The surface tension coefficients σ_i at the interface Γ_i ($i=1, 2$) are also constant.

As usual in modelling gas–liquid free surfaces, the gas is assumed to be incompressible and ideal, i.e. inviscid, and the pressure in the gas phase to be a constant with respect to the space variable:[9,25]

$$p_0 = p_0(t). \tag{1}$$

Remark 1. The function $p_0(t)$ is determined from the condition that the volume of the gas phase is constant in time. Hence $p_0(t)$ has not to be specified; it is a Lagrangian multiplier for this

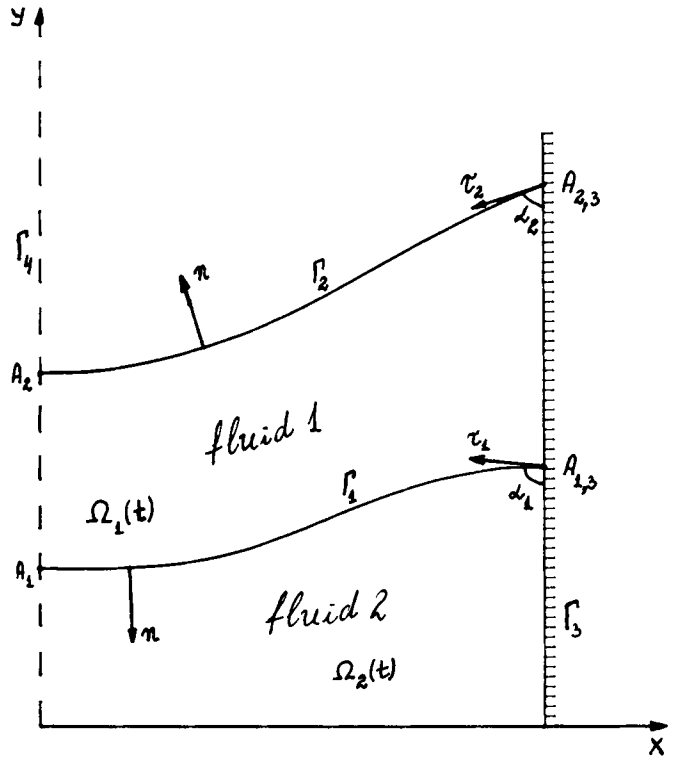

Figure 1. Sketch of principles of free surface problems

condition. Naturally, if $p_0(t)$ has an arbitrary value then the volume of the gas phase will expand or diminish. This approach has been used also in the numerical solution of stationary problems.[10]

For each liquid phase we write the Navier–Stokes equations in dimensionless form:[18,25]

$$\mathrm{D}\mathbf{V}^{(1)}/\mathrm{D}t = \nabla\cdot\mathbb{T}^{(1)} - \nabla p^{(1)} + \mathbf{F}^{(1)}, \qquad \nabla\cdot\mathbf{V}^{(1)} = 0, \tag{2}$$

$$\lambda\mathrm{D}\mathbf{V}^{(2)}/\mathrm{D}t = \nabla\cdot\mathbb{T}^{(2)} - \nabla p^{(2)} + \mathbf{F}^{(2)}, \qquad \nabla\cdot\mathbf{V}^{(2)} = 0, \tag{3}$$

where $\mathbf{V}^{(s)}(u^{(s)}, v^{(s)})$, $p^{(s)}$ and $\mathbf{F}^{(s)}$ are respectively the velocity, pressure and body forces in the sth liquid, $\mathrm{D}/\mathrm{D}t = \partial_t + (\mathbf{V}\cdot\nabla)$ and $\lambda = \rho_2/\rho_1$. We consider this equations for the 2D plane and axisymmetric cases.

We study here only the case of Newtonian liquids for which

$$\mathbb{T}^{(1)} = Re^{-1}\,\mathbb{D}(\mathbf{V}^{(1)}), \qquad \mathbb{T}^{(2)} = \eta Re^{-1}\,\mathbb{D}(\mathbf{V}^{(2)}), \tag{4}$$

where $\mathbb{D}_{kj}(\mathbf{V}^{(i)}) = 0{\cdot}5(\partial_k \mathbf{V}_j^{(i)} + \partial_j \mathbf{V}_k^{(i)})$, $i = 1, 2$, is the shear stress tensor, $\eta = \mu_2/\mu_1$, $Re = U_0 l\rho_1/\mu_1$, U_0 is the reference velocity and l is the reference length.

We shall refer to the liquid–liquid interface as the first one and to the gas–liquid interface as the second one (see Figure 1). We write their equations in the form $S_i(\mathbf{X}, t) = 0$, $i = 1, 2$.

For the free surfaces we write the standard kinematic condition[25]

$$\mathrm{D}S_i/\mathrm{D}t = 0. \tag{5}$$

On the liquid–liquid free surface Γ_1 the standard boundary conditions are obtained from the full surface forces balance and the continuity of the velocity field across the boundary:[13]

$$\mathbb{T}^{(1)}\cdot n-\mathbb{T}^{(2)}\cdot n+(p^{(2)}-p^{(1)})n-\mathbf{R}_1|_{\Gamma_1}=0, \qquad (\mathbf{V}^{(1)}-\mathbf{V}^{(2)})|_{\Gamma_1}=0, \tag{6a, b}$$

where n is the unit normal to Γ_1 and $\mathbf{R}_1$ is the vector of surface forces at Γ_1. If we take in (6) the unit outward normal to Ω_2 then the vector $\mathbf{R}_1$ has to be taken with the opposite direction. The condition (6a) means that the stress tensor jump over the free boundary is equal to the vector of the internal interface forces. Naturally it consists of two scalar conditions in the 2D case—say balance of the forces normal to the interface and of those tangential to it. If the surface force $\mathbf{R}_1$ is directed perpendicularly to the interface as the surface tension one (13) then the boundary condition (6a) implies continuity of shear stresses across the free boundary.

In the gas phase the stress tensor reduces to the internal pressure and so at the gas–liquid interface (6a) reads

$$\mathbb{T}^{(1)}\cdot n+(p_0-p^{(1)})n-\mathbf{R}_2|_{\Gamma_2}=0, \tag{7}$$

where n is the unit outward normal to Ω_2 and $\mathbf{R}_2$ is the vector of surface forces at Γ_2.

At infinity and at the rigid boundaries (see Figure 1) the standard no-slip conditions are applied:

$$\mathbf{V}|_{\Gamma_3}=\mathbf{V}_g, \qquad \mathbf{V}_g \text{ is a known function.} \tag{8}$$

The function $\mathbf{V}_g$ in the boundary condition is equal to the velocity of the rigid interface motion. Naturally it is zero at quiescent walls.

The standard symmetry boundary conditions are used on the line of symmetry Γ_4. If it is the axis y, they read

$$u(x, y)=-u(-x, y), \qquad v(x, y)=v(-x, y), \qquad p(x, y)=p(-x, y). \tag{9}$$

The symmetry condition at the cross-point A_i of the free surface Γ_i and Γ_4 is standard:

$$S_i(x, y)=S_i(-x, y), \quad i=1, 2. \tag{10}$$

We use the symmetry conditions to derive the principle of virtual work in Section 3 in the form (9) and (10), but they can also be formulated equivalently as

$$u|_{\Gamma_4}=0, \qquad \partial v/\partial x|_{\Gamma_4}=0, \qquad \partial p/\partial x|_{\Gamma_4}=0, \qquad \partial S/\partial x|_{\Gamma_4}=0.$$

The initial conditions for the velocity and the position of the free boundaries are of the form

$$\mathbf{V}|_{t=0}=\mathbf{V}_0, \qquad S_i|_{t=0}=S_{i,0}, \quad i=1, 2. \tag{11}$$

Here we consider only gravity and surface tension as examples of body and surface forces respectively:

$$\mathbf{F}_s=\operatorname{grad} H_s, \quad s=1, 2, \qquad H_1=-Fr^{-1}y, \qquad Fr=U_0^2/gl, \qquad H_2=\lambda H_1, \tag{12}$$

$$R_2=(1/We)(1/R_1+1/R_2)\bar{n}, \qquad We=U_0\rho l/\sigma_1, \qquad \mathbf{R}_1=\kappa\mathbf{R}_2, \qquad \kappa=\sigma_2/\sigma_1. \tag{13}$$

The direction of the gravity force is assumed to be opposite to the direction of the axis y, R_1 and R_2 are the two main radii of curvature, g is the gravitational acceleration and $\bar{n}$ is the unit normal pointing to the centre of curvature.

At the contact points (if any) of two interfaces (in our case a free surface Γ_1 or Γ_2 with a rigid body surface Γ_3) the specification of the contact angle is required:[6, 29]

$$\tau(A_{1,3})=\alpha^{1,3}, \qquad \tau(A_{2,3})=\alpha^{2,3}, \tag{14}$$

where τ is the unit positive tangent to Ω_1 (i.e. its direction indicates anticlockwise bypass of Ω_1), $\alpha^{i,j}$ are known vectors and $A_{i,j}$ are points from $\Gamma_i \cap \Gamma_j$. This is necessary only if surface tension is present at the interface.

At the line of symmetry the condition (10) yields

$$\tau(A_4)=(1, 0). \tag{15}$$

3. NUMERICAL METHOD

3.1. Principle of virtual work and initial system of equations

The principle of virtual work is used to discretize the equations formulated in the previous section in space.[18] This is the Galerkin formulation of equations (2)–(4) and (6)–(10) and in our case it reads

$$\int_{\Omega_1(t)} [(\mathrm{D}\mathbf{V}^{(1)}/\mathrm{D}t)\cdot\delta\mathbf{V}^{(1)} + Re^{-1}\,\mathbb{D}(\mathbf{V}^{(1)})\cdot\mathbb{D}(\delta\mathbf{V}^{(1)}) - p^{(1)}\nabla\cdot\delta\mathbf{V}^{(1)} - \mathbf{F}^{(1)}\cdot\delta\mathbf{V}^{(1)}]\,\mathrm{d}\Omega$$

$$+\int_{\Omega_2(t)} [\lambda(\mathrm{D}\mathbf{V}^{(2)}/\mathrm{D}t)\cdot\delta\mathbf{V}^{(2)} + \eta Re^{-1}\,\mathbb{D}(\mathbf{V}^{(2)})\cdot\mathbb{D}(\delta\mathbf{V}^{(2)}) - p^{(2)}\nabla\cdot\mathbf{V}^{(2)} - \mathbf{F}^{(2)}\cdot\delta\mathbf{V}^{(2)}]\,\mathrm{d}\Omega$$

$$= \int_{\Gamma_1} \mathbf{R}_1\cdot\delta\mathbf{V}^{(1)}\,\mathrm{d}s + \int_{\Gamma_2} \mathbf{R}_2\cdot\delta\mathbf{V}^{(2)}\,\mathrm{d}s + \int_{\Gamma_2} p_0\,\delta\mathbf{V}^{(1)}\cdot n\,\mathrm{d}s,$$

$$\mathbf{V}^{(1)} - \mathbf{V}^{(2)}|_{\Gamma_2} = 0, \qquad \mathbf{V}^{(s)} \in \mathbb{V}_g^{(s)}, \quad \delta\mathbf{V}^{(s)} \in \mathbb{V}_0^{(s)}, \quad p^{(s)}, \delta p^{(s)} \in \mathbb{M}^{(s)}, \quad s=1, 2, \tag{16}$$

$$\int_{\Omega_1(t)} \nabla\cdot\mathbf{V}^{(1)}\,\delta p^{(1)}\,\mathrm{d}\Omega + \int_{\Omega_2(t)} \nabla\cdot\mathbf{V}^{(2)}\,\delta p^{(2)}\,\mathrm{d}\Omega = 0, \tag{17}$$

where $\mathrm{d}\Omega = \mathrm{d}x\,\mathrm{d}y$, $\mathrm{d}s = (\dot{x}^2+\dot{y}^2)^{1/2}\,\mathrm{d}q$, $x=x(q)$ and $y=y(q)$ in the plane case and $\mathrm{d}\Omega = x\,\mathrm{d}x\,\mathrm{d}y$ and $\mathrm{d}s = x(\dot{x}^2+\dot{y}^2)^{1/2}\,\mathrm{d}q$ in the axisymmetric case. The orthogonal co-ordinate system is Oxy and in the axisymmetric case x plays the role of the polar radius r. The spaces $\mathbb{V}_g^{(s)}$ and $\mathbb{M}^{(s)}$ are subspaces of $H_1(\Omega_s(t))^n$, $n=2, 3$, and $L_2(\Omega_s(t))$ respectively, $s=1, 2$.

In order to derive (16), the momentum equation for the first (resp. second) liquid phase (2a) (resp. (3a)) is multiplied by the velocity variation $\delta\mathbf{V}^{(1)}$ (resp. $\delta\mathbf{V}^{(2)}$) and integrated over $\Omega_1(t)$ (resp. $\Omega_2(t)$); the two parts are then added together. Integrating by parts over $\Omega_1(t)$ and $\Omega_2(t)$ and using the surface force balance conditions (6a) and (7), we get (16). The condition (17) is obtained in the same way without integration by parts. The velocity continuity condition (6b) and the essential boundary conditions for the velocity (8) are included in the definition of the velocity admissible functions in the standard way.[18]

If the problem is symmetric with respect to a line then it is convenient to use (16) and (17) in a half-domain. If the line of symmetry is the axis y then $\Omega_1(t)$, $\Omega_2(t)$, $\Gamma_1(t)$ and $\Gamma_2(t)$ have to be substituted in (16) and (17) with their intersection with the half-plane $\{\mathbf{X}(x, y): x>0\}$. The symmetry conditions (9) and (10) are used to motivate this operation.

Consider a finite element approximation for the velocity and pressure:

$$\mathbf{V}_h = \sum U_i\Phi_i, \qquad p_h = \sum P_k\Pi_k, \tag{18}$$

where U_i are nodal unknowns for the velocity and P_k are unknowns for the pressure.

Below we state the admissibility conditions for conforming finite elements for the Galerkin formulation (16) and (17). The velocity approximation has to be continuous in $\Omega(t)=\Omega_1(t)\cup\Omega_2(t)$.

The essential BCs (8) for the velocity have to be applied on $\mathbf{V}_h$. For the pressure approximation, discontinuities at the finite element interfaces are allowed. In our case this is very convenient since the pressure is physically discontinuous over the deformable interface. For the pressure no essential boundary conditions are required except its value at one fixed point. In all examples considered here this will be the point of truncated infinity at the line y.

We employ the quadrilateral isoparametric Q_2/P_1 finite element introduced by Engelman *et al.*[30] and recommended by Fortin *et al.*[31] and Cliffe and Lever.[32] It possesses nine nodes for velocity and linear discontinuous pressure:

$$\mathbf{V}_h(\xi,\eta)=\sum_{i=1}^{9}\Phi_i(\xi,\eta)\mathbf{v}_i, \qquad p_h(\xi,\eta)=p_0+p_1\xi+p_2\eta, \tag{19a,b}$$

where ξ and η are the local co-ordinates in the standard reference square $[-1,1]\times[-1,1]$.

It is convenient to introduce notations for the functions and coefficients in the whole computational domain using the characteristic function X_s of $\Omega_s(t)$, $s=1,2$:

$$\mathbf{V}(\mathbf{X})=\mathbf{V}^{(1)}(\mathbf{X})X_1(\mathbf{X})+\mathbf{V}^{(2)}(\mathbf{X})X_2(\mathbf{X}), \qquad p(\mathbf{X})=p^{(1)}(\mathbf{X})X_1(\mathbf{X})+p^{(2)}(\mathbf{X})X_2(\mathbf{X}),$$

$$\mathbf{F}=\mathbf{F}_1X_1+\mathbf{F}_2X_2, \qquad \hat{\lambda}=1\cdot X_1+\lambda X_2, \qquad \hat{\mu}=Re^{-1}X_1+\eta Re^{-1}X_2(\mathbf{X}).$$

To obtain a semidiscrete FEM system of equations from (16) and (17), it is enough to use for $\delta\mathbf{V}$ the basis functions Φ_i and for δp the basis functions Π_k:

$$\int_{\Omega(t)}[\hat{\lambda}(\mathrm{D}\mathbf{V}_h/\mathrm{D}T)\cdot\Phi_j+\hat{\mu}\mathbb{D}(\mathbf{V}_h)\cdot\mathbb{D}(\Phi_j)-p_h\nabla\Phi_j-\mathbf{F}\cdot\Phi_j]\,\mathrm{d}\Omega=\varphi_1(\Phi_j)+\varphi_2(\Phi_j)+\varphi_0(\Phi_j), \tag{20}$$

$$\int_{\Omega(t)}\nabla\cdot\mathbf{V}_h\Pi_k\,\mathrm{d}\Omega=0, \tag{21}$$

where

$$\varphi_1(\Phi_j)=\int_{\Gamma_1}\mathbf{R}_1\Phi_j\,\mathrm{d}s, \qquad \varphi_2(\Phi_j)=\int_{\Gamma_2}\mathbf{R}_2\Phi_j\,\mathrm{d}s, \qquad \varphi_0(\Phi_j)=p_0\int_{\Gamma_2}\Phi_j\cdot n\,\mathrm{d}s.$$

The functionals φ_1 and φ_2 represent the contribution of the surface tension and are computed directly. This yields nearly the same results as the method of Ruschak[33] but the former is more convenient for us because of some programming reasons.

We apply the fully implicit scheme in combination with the Lagrangian approach to discretize the full time derivative in (20) and (21). At the time moment t the resulting linear system is

$$\tau^{-1}\mathbb{M}(U-U_{\mathrm{L}})+\mathbb{A}U-\mathbb{B}^{\mathrm{T}}P=\mathbb{F}, \qquad \mathbb{B}U=0, \qquad U=\{U_i\}, \qquad P=\{P_k\}, \tag{22a–d}$$

$$\mathbb{M}_{i,j}=\int_{\Omega(t)}\hat{\lambda}\Phi_i\cdot\Phi_j\,\mathrm{d}\Omega, \qquad \mathbb{A}_{i,j}=\int_{\Omega(t)}\hat{\mu}\mathbb{D}(\Phi_i)\cdot\mathbb{D}(\Phi_j)\,\mathrm{d}\Omega,$$

$$\mathbb{F}_j=\int_{\Omega(t)}\mathbf{F}\cdot\Phi_j\,\mathrm{d}\Omega+\varphi_1(\Phi_j)+\varphi_2(\Phi_j)+\varphi_0(\Phi_j), \qquad \mathbb{B}_{i,k}=\int_{\Omega(t)}\nabla\cdot\Phi_i\Pi_k\,\mathrm{d}\Omega. \tag{23}$$

The vector U_{L} of the velocity unknowns at the previous positions of the mesh points is defined as

$$\mathbf{X}(t)=\mathbf{X}(t-\tau)+\tau\mathbf{V}(t-\tau), \qquad \mathbf{V}(t-\tau)=\sum U_{\mathrm{L},i}\Phi_i(t-\tau). \tag{24}$$

Remark 2. As mentioned before, $p_0(t)$ is unknown and hence the RHS of (20) and (23) is known up to a constant. This difficulty is overcome in an elegant way in the next subsection.

3.2. FEs in internal variables

The systems of equations (22) is partially solved during the stage of computing of the local matrices and assembled as described by Shopov.[34] This procedure is similar to the divergence-free approach,[21] but the numerical method is still considered as a velocity–pressure one. We shall sketch it here because this information is essential for the grid redefinition step and for the elimination of the function $p_0(t)$.

The velocity unknowns $\{U\}$ are partitioned into two classes, basis (internal) ones $\{\tilde{U}\}$ and non-basis ones $\{\tilde{\tilde{U}}\}$:

$$\{U\}=\{\tilde{U}\}\cup\{\tilde{\tilde{U}}\}, \qquad \{\tilde{U}\}\cap\{\tilde{\tilde{U}}\}=0. \tag{25}$$

Roughly speaking, $\tilde{\tilde{U}}$ are the unknowns which can be expressed by the incompressibility condition (22b).

We solve systems only for internal variables, which comprise about half the overall unknowns (i.e. unknowns for the velocity and pressure). Knowing these, we can calculate by a simple explicit formula the full set of overall unknowns. The full set of velocity unknowns (except those at the centroid of every FE) are required at the Lagrangian time step.

The partitioning of the unknowns is realized in three steps. These are performed by means of simple operations on the shape matrices $\mathbb{H}$:

$$\mathbf{V}_h=\mathbb{H}\cdot P, \qquad P=\{1,\xi,\eta,\xi^2,\xi\eta,\eta^2,\xi^2\eta,\xi\eta^2,\xi^2\eta^2\} \tag{26}$$

First, the evidently non-basis unknowns are the velocities u_0 and v_0 at the centroid of the finite element and they are expressed through $(u_1, v_1, \ldots, u_B, v_B)$ from (22b). Substituting these unknowns in the velocity approximation, we obtain a new form of the initial finite element; the pressure is approximated by a constant. This procedure is applied by many authors.[21,31,35]

$$\{u_0, v_0\}\in\{\tilde{\tilde{U}}\}, \qquad (u_0, v_0)=C\{u_i, v_i, u_{i,i+1}, v_{i,i+1}\}. \tag{27}$$

Practically, this is an algorithm to eliminate $\{u_0\}$ and $\{v_0\}$ from (22b) and $\{p_1\}$ and $\{p_2\}$ from (22a). It is performed at local level before assembling the local matrices.

Next we have to separate from the remaining variables the remaining non-basis ones. For this operation we have to change the variables $(u_{i,i+1}, v_{i,i+1})$ at the midpoints of the sides with the circulation and the flux variables for the curvilinear side, $a_i=(P_iP_{i,i+1}P_{i+1})$:

$$C_i=\int_{a_i}\mathbf{V}_h\cdot\tau\,\mathrm{d}s, \qquad Q_i=\int_{a_i}\mathbf{V}_h\cdot n\,\mathrm{d}s, \tag{28}$$

where the tangent is arbitrary but fixed at the global level for every finite element side. This choice is performed automatically in the programme code and recorded in an appropriate way. The normals in (28) are obtained by rotation of the tangents to the angle $-\pi/2$. This is the second step. All circulation variables are basis (internal) ones. They are of the order $O(h)$ so we norm them:

$$G_i=\|\bar{a}_i\|^{-1}C_i, \qquad \bar{a}_i=(P_iP_{i+1}) \quad \text{(a linear segment)}, \tag{29}$$

which physically means that G-variables are averaged tangential velocities along the sides.

The third step is to divide the flux variables into internal and non-basis ones. To do this, we employ an implicit algorithm based on the mesh streamfunction, defined as

$$\Psi_{i+1}=\Psi_i+Q_i, \tag{30}$$

where the notations are local; the normal in the evaluation of Q_i is the local positive tangent rotated to $-\pi/2$.

Using (22b), it is easy to see that (30) is a correct recursive definition. The last change of variables is

$$Q_i = \Psi_{i+1} - \Psi_i. \tag{31}$$

The internal variables are

$$\{\tilde{U}\} = \{u_i\} \cup \{v_i\} \cup \{G_i\} \cup \{\Psi_i\}. \tag{32}$$

As a result of these operations we obtain a new approximation in which the parameters are only internal variables, (see Figure 2):

$$\tilde{\mathbf{V}}_h = \sum \tilde{U}_i \tilde{\Phi}_i. \tag{33}$$

After eliminating the non-basis variables from the system (22) by an appropriate algorithm,[34] we obtain a new equivalent system in internal variables

$$\tau^{-1} \tilde{\mathbb{M}} (\tilde{U} - \tilde{U}_L) + \tilde{\mathbb{A}} \tilde{U} = \tilde{\mathbb{F}}. \tag{34}$$

Both matrices $\tilde{\mathbb{M}}$ and $\tilde{\mathbb{A}}$ are positive definite and symmetric. This system corresponds formally to the principle of virtual work (16) with the zero-pressure approximation:

$$\int_{\Omega(t)} \tilde{\lambda} (\tilde{\mathbf{D}} \mathbf{V}_h / \mathrm{D}t) \cdot \tilde{\Phi}_j + \hat{\mu} \tilde{\tilde{\mathbb{T}}} \mathbf{V}_h \cdot \tilde{\mathbb{D}} \Phi_j - \mathbf{F} \cdot \tilde{\Phi}_j \, \mathrm{d}\Omega = \varphi_1(\tilde{\Phi}_j) + \varphi_2(\tilde{\Phi}_j), \tag{35}$$

and zero gas pressure constant, $p_0(t) = 0$.

Remark 3. The functional φ_0 is absent from (35) because its contributions cancel each other during transformations from (22) to (34), or equivalently,

$$\varphi_0(\tilde{\Phi}_j) \equiv 0 \tag{36}$$

owing to the construction of $\tilde{\Phi}_j$; for the specific form of $\tilde{\Phi}_j$ see Reference 34.

Thus, using the internal variables procedure for solving the system of equations, we are able to eliminate the difficulty with the unknown function $p_0(t)$. From the physical point of view this is also natural because the volume of the gas phase is automatically constant in time owing to the incompressibility of the ambient liquid (this is automatically imposed by the divergence-free principle of virtual work (35) and hence the Lagrangian multiplier for this condition is redundant.

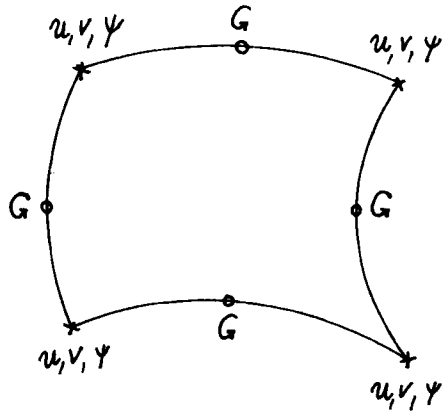

Figure 2. FE in internal variables

The systems (34) can be treated in various ways. We usually apply a variant of the square root method for band-symmetric positive definite matrices from Reference 18. Our systems involve a moderate number of unknowns and the computer time expenses are reasonable. We also employ the successive overrelaxation method. The acceleration parameter is taken to be 1·41 and this value is obtained experimentally. The computer efficiency of both methods appears to be nearly the same. The iterations are stopped if two successive iterations differ by less then 5×10^{-5} in the uniform norm. The employment of more efficient iterative methods is advisable since we have in hand a good initial guess for the unknown vector.

The described algorithm for the system (22) possesses a couple of advantages. The number of unknowns is substantially reduced. The systems obtained are positive definite with a modest number of unknowns and this allows us to treat them in a simple way. The unknown pressure in the gas phase is eliminated from the system of equations to be solved. The incompressibility condition (22b) is satisfied identically and exact mass conservation holds at every time level. In the course of the computations we also obtain the streamfunction, which is useful for mechanical representation and interpretation of the results.

Of course, other methods can also be applied to treat the initial system (22). Usava iteration or penalization techniques could be employed to satisfy (22b), but in this case some additional problems with the functional φ_0 remain.

3.3. Grid redefinition

A typical feature of Lagrangian methods is that they require a regridding, which can be performed in three basic steps (see e.g. Reference 20 and references cited therein). For divergence-free methods an additional fourth step is necessary.

(i) Define a new conforming triangulation $\mathscr{T}_h$ with nodes $\{A_i\}$.
(ii) For every A_i find FE e'_j from the old triangulation $\mathscr{T}'_h$ so that $A_i \in e'_j$.
(iii) Find $\mathbf{V}(A_i) = \mathbf{V}'_{h,e'}(A_i)$ using the old velocity field $\mathbf{V}'_h$ at $\mathscr{T}'_h$. In this way the new velocity field $\mathbf{V}_h$ at $\mathscr{T}_h$ is defined.
(iv) Define a discretely divergence-free approximation $\bar{\mathbf{V}}_h$ of $\mathbf{V}_h$ at the triangulation $\mathscr{T}_h$, i.e. $\bar{\mathbf{V}}_h$ has to satisfy (17) or, equivalently, (22b).

The first three steps are performed in the general frame of the standard approach[20,25] with some small differences in the algorithms[27] whose description here seems unnecessary.

To perform the last step, we use the residual $R(\mathbf{V}, \mathscr{T}_h)$ in (17) for the velocity field $\mathbf{V}$ as a practical measure of the deviation of $\mathbf{V}$ from a discretely divergence-free one at the triangulation $\mathscr{T}_h$:

$$\sum_{\mathbf{A}_e} Q_e(\mathbf{V}, a_i) = r_e, \qquad \mathbf{A}_e = \{a_i; a_i \subset \partial e\}, \qquad \max |r_e| = R(\mathbf{V}, \mathscr{T}_h), \qquad e \in \mathscr{T}_h, \tag{37}$$

where Q_e is the flux through the side a_i of the element e with respect to the external normal. Evidently the vector field $\mathbf{V}_h$, or equivalently the vector of the nodal variables $\{\mathbf{V}(A_i)\} = V$ (without variables at the centroids), is discretely divergence-free at the triangulation $\mathscr{T}_h$ iff $R(\mathbf{V}, \mathscr{T}_h) = 0$.

By construction the old velocity field $\mathbf{V}'_h$ is divergence-free at the old triangulation $\mathscr{T}'_h$, but in general this is not true for the new triangulation $\mathscr{T}_h$:

$$R(\mathbf{V}'_h, \mathscr{T}'_h) = 0, \qquad R(\mathbf{V}'_h, \mathscr{T}_h) = O(h^2). \tag{38}$$

The field V calculated at $\mathscr{T}_h$ from any set of internal variables $\{U_i^1\}$ (see Section 3.2) is discretely divergence-free at $\mathscr{T}_h$ and conversely a velocity field $\mathbf{V}$ could be generated by a set of internal variables iff $R(\mathbf{V}, \mathscr{T}_h)=0$. To produce a divergence-free approximation from the set of velocity variables $\{\mathbf{V}(A_j)\}=V$ in practice means to perform some changes in the velocity variables at the mid-side nodes $\{\mathbf{V}(A_{i,i+1})\}=V^{\mathrm{M}}\subset V$ in order to achieve $R(\mathbf{V}_h, \mathscr{T}_h)=0$.

One possibility is to alter all variables $\{\mathbf{V}(A_{i,i+1})\}$ by choosing new values $\{\bar{\mathbf{V}}(A_{i,i+1})\}=\{\bar{V}_s^{\mathrm{M}}\}_{s=1}^n$ for them as close as possible to the initial ones, say in the discrete least square norm, i.e.

$$\min \sum_{s=1}^{n} q_s |V_s^{\mathrm{M}}-\bar{V}_s^{\mathrm{M}}|^2, \qquad \mathbb{B}\bar{V}=0, \tag{39a, b}$$

where q_s are weights which determine the admissible deviation of the initial value. This is a standard problem to be solved but one specific difficulty remains. Our experiments show that the numerical method is very sensitive to changes in the velocity variables at the free boundary and we have to use large weights q_s for such variables.

Thus in practice we proceed in a simpler way by just preserving some chosen velocities at $n-m$ mid-side points (all such points belonging to the free boundary are among them) and computing the others from (39b). Of course, this choice cannot be arbitrary because it is equivalent to choosing a set of internal variables (in general this set is different from the one fixed in Section 3.2 and used in (34)) or a set of fluxes for computing the mesh streamfunction.[34]

To find $\bar{V}$ in this way means to compute one presentation of V in internal variables (this is not unique, of course) and then to go back to the primitive ones. Such a procedure needs no extra programming because it is the same as the implementation of the initial conditions.

The numerical experiments show the importance of the preservation of velocities at the free boundaries. Thus always include them in the basis and the values of the mesh streamfunction are preserved there. Next the mesh streamfunction is calculated consecutively by layers, first at neighbouring points to the boundaries (first layer) using the fluxes through the sides with one end at the interface. In this way the mesh streamfunction is defined at the first layer and this procedure is repeated recursively for the second layer and so on. We also experimented with other algorithms to choose the basic set of fluxes based on the assumption that the accuracy is worse in the regions with greater velocity gradients, but the results did not improve with respect to this simple one. Perhaps this is connected with the type of our problems, for which the quality of the approximation near the free boundary is crucial.

It is easy to see that

$$\|\mathbf{V}_h-\bar{\mathbf{V}}_h\|_1=O(h^2), \tag{40}$$

and hence the asymptotic accuracy of the method will not be affected.

As a measure of the quality of the new approximation $\bar{\mathbf{V}}_h$ we use its distance from $\mathbf{V}$ in the mesh uniform norm:

$$RR(\mathbf{V}, \mathscr{T}_h)=\max|\mathbf{V}(A_i)-\bar{\mathbf{V}}(A_i)|/\max|\mathbf{V}(A_i)|, \quad A_i\in\mathscr{T}_h. \tag{41}$$

The accuracy of this regridding algorithm is tested on both the analytical solution $\mathbf{V}^{\mathrm{ex}}$ of the Stokes flow past a unit sphere[36] and the finite element solution $\mathbf{V}_h^{\mathrm{apr}}$ of the same problem obtained as outlined in Sections 3.1 and 3.2. The field $\mathbf{V}_h^{\mathrm{apr}}$ is obtained in internal variables and afterwards is converted to the initial variables form (19a); hence it is discretely divergence-free at the triangulation $\mathscr{T}_h'$. The other test function—the standard finite element interpolant of the exact solution, $\mathbf{V}_{1,h}^{\mathrm{ex}}$—is not discretely divergence-free at the triangulation $\mathscr{T}_h'$.

Both $\mathbf{V}_h^{\mathrm{apr}}$ and $\mathbf{V}_{1,h}^{\mathrm{ex}}$ are considered on two uniform meashes $\mathscr{T}'_{1,h}$ and $\mathscr{T}'_{2,h}$ with four and 16 finite elements respectively in a quarter-domain and truncated infinity at five sphere radii from

the body. Using the previously described algorithm, these velocity fields are employed to define the velocity field $\mathbf{V}_h$ on a new mesh $\mathscr{T}_h$ and its divergence-free approximation $\bar{\mathbf{V}}_h$ at $\mathscr{T}_h$.

We consider two new meshes $\mathscr{T}_{1,h}$ and $\mathscr{T}_{2,h}$ which are non-uniform in the radial direction in the proportions 1:2 and 1:2:3:4 respectively. The distance of $\bar{\mathbf{V}}_h$ and the corresponding mesh streamfunction Ψ_h from the exact solution $(\mathbf{V}^{ex}, \Psi^{ex})$ is studied as well as the distance $RR(\mathbf{V}_h, \mathscr{T}'_h)$ of $\bar{\mathbf{V}}_h$ from the initial field $\mathbf{V}_h$.

The results are given in Table I: the first two rows contain data for $\bar{\mathbf{V}}_h^{ex}$ at $\mathscr{T}_{1,h}$ and $\mathscr{T}_{2,h}$ constructed from $\mathbf{V}^{ex}$ at $\mathscr{T}'_{1,h}$ and $\mathscr{T}'_{2,h}$; the last two rows contains the same information for $\bar{\mathbf{V}}_h^{apr}$. Data for the deviation $R(\mathbf{V}_h, \mathscr{T}_h)$ of the initial interpolant $\mathbf{V}_h$ from the discretely divergence-free field $\bar{\mathbf{V}}_h$ are also presented.

It is clear that the FEM solution is not considerably worse then the exact one with respect to the regridding procedure. The convergence tendency is clearly visible. The accuracy for the streamfunction is much better than for the velocity because it converges as $O(h^3)$ in the uniform norm.[37]

3.4. Free surface computation and automatic choice of the time integration step

Consider one of the interfaces Γ with the equation $S(\mathbf{x}, t)=0$. A natural predictor step follows from the kinematic condition (5):

$$\mathbf{x}^p(\hat{t})=\mathbf{x}(t)+\Delta t\,\mathbf{v}^p(t)+O(\Delta t^2), \qquad \mathbf{v}^p(t)=\mathbf{v}(\mathbf{x}(t), t). \tag{42}$$

The problem (22) is solved in $\Omega^p(\hat{t})$ to obtain the new velocity $\mathbf{v}^c(\mathbf{x}, \hat{t})$. Then the correction is constructed:

$$\mathbf{x}^c(\hat{t})=\mathbf{x}(t)+\Delta t\,\mathbf{v}^c(t) \quad \text{or} \quad \mathbf{x}^c(\hat{t})=\mathbf{x}(t)+0{\cdot}5\,\Delta t(\mathbf{v}^c(t)+\mathbf{v}^p(t)). \tag{43a, b}$$

The second equation has a truncation error $O(\Delta t^3)$ if $\mathbf{v}^p(t)$ and $\mathbf{v}^c(t)$ are computed exactly and has proved experimentally to be better.

Many authors have applied a fixed time integration step. This is a reasonable solution if we can work with small Δt. First we tried to work in this way but two main problems arose: spurious instability of the free boundary occurred and even non-physical non-smooth shapes (e.g. high peaks adjacent to deep valleys). Often the integration process goes well for a time period but after that the results are obviously non-physical. The computations have to be repeated with a smaller time step, but for different stages of the studied mechanical problems this requirement changes. Such experience forced us to develop the adaptive time-stepping algorithm.

Let ε be the total accuracy required for the evaluation of the free boundary. Then at every time step the following condition has to be satisfied:

$$|\mathbf{x}^c(q)-\mathbf{x}^p(q)|_c<\varepsilon\Delta t, \tag{44}$$

where $\mathbf{x}(q)$ is the parameterization of Γ (see equation (56)).

Table I

Elements	$\lvert\bar{\mathbf{V}}_h-\mathbf{V}^{ex}\rvert_c$	$\lvert\bar{\psi}_h-\psi^{ex}\rvert_c$	$R(\mathbf{V}_h, \mathscr{T}_h)$
4	6·3%	10·55%	6·373%
16	4·2%	1·97%	2·22%
4	6·9%	12·25%	5·88%
16	4·5%	2·2%	3%

This condition is equivalent to similar conditions on the velocity. For correction (43b) it reads as

$$|\mathbf{v}^{\mathrm{p}}(q)-\mathbf{v}^{\mathrm{c}}(q)|_{\mathrm{c}}<2\varepsilon. \tag{45}$$

Practically this control is on the tangential and normal components of velocity, but the tangential velocity is not connected essentially with the displacement of the interface.

To illustrate this, we consider the motion of S in the Eulerian approach. The kinematic condition (3) can be written in the form

$$\partial_t S+(\operatorname{grad} S, \mathbf{v})=0 \tag{46a}$$

or

$$\partial_t S \| N \|^{-1}=-\mathbf{v}\cdot n, \qquad N=(\partial_1 S, \partial_2 S), \qquad n=N/\| N \|. \tag{46b}$$

Hence theoretically the tangential velocity does not influence the displacement of the interface. In the Lagrangian approach this is true only with $O(\Delta t^2)$ because the tangent to the old boundary differs from the tangent to the new one with $O(\Delta t)$.

This can be explained as follows. Let us decompose, for example, the step (42) into two components, i.e. the normal displacement of the boundary, corresponding to (46), and the tangential one:

$$\bar{S}_h: \quad \bar{\mathbf{x}}(\hat{t})=\mathbf{x}(t)+\Delta t\mathbf{v}^{\mathrm{p}}(t)\cdot n(t). \tag{47}$$

This step determines the new position of the boundary. Next we have to determine the new position of the mesh points at the interface. Hence the next step is

$$\mathbf{x}(\hat{t})=\bar{\mathbf{x}}(\hat{t})+\Delta t\,\mathbf{v}^{\mathrm{p}}(t)\cdot\tau(t). \tag{48}$$

The two steps (47) and (48) are equivalent to (42). The curves (47) and (42) differ by $O(\Delta t^2)$ (see Figure 3). To force them to coincide, we can project the point $\hat{A}$ on $\bar{S}_h$. We skip this operation owing to its relative complexity and consider (42) as an approximation for (47) and (48).

Numerical experiments also prove that controlling only the normal component yields better results than (45). If the following inequality is satisfied,

$$|\mathbf{v}^{\mathrm{p}}\cdot n(q)-\mathbf{v}^{\mathrm{c}}\cdot n(q)|_{\mathrm{c}}=R(t)<2\varepsilon, \tag{49}$$

then the step is considered to be legal. The new position of the boundary is determined by (43b) and by

$$\mathbf{v}(\hat{t})=0{\cdot}5(\mathbf{v}^{\mathrm{p}}(t)+\mathbf{v}^{\mathrm{c}}(t)). \tag{50}$$

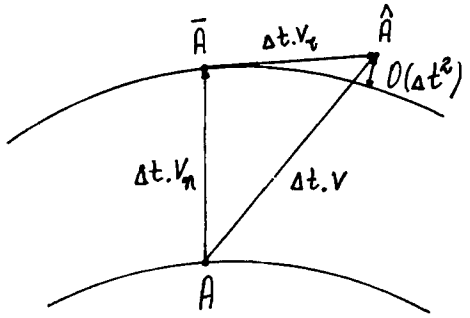

Figure 3. Motion of free boundary

If $R(t)>2\varepsilon$, the step is considered illegal, Δt is cut down to $\Delta t/2$ and the procedure is repeated.

If $R(t)<\varepsilon$, then time step Δt is increased to $2\Delta t$. The absolute maximum value $\Delta t_{\max}$ is previously defined to prevent an eventual infinite increase of the time integration step.

We also control the smoothness of Γ_h. The maximum of the angle $\theta_0=2\pi-\theta$ is measured and controlled:

$$\max\theta_0<\theta_{\max}, \qquad \theta_0=2\pi-\theta, \tag{51}$$

where θ is the angle between the segments of the free boundary.

If this angle is too large without a physical singularity at the point then the computed free boundary is also considered illegal. Both predictor and corrector steps are controlled. If (51) is not fulfilled then the step is rejected and Δt is decreased.

The value of $\theta_{\max}$ is usually taken to be about 11° in our numerical experiments.

If the interface is not stable or the method is losing accuracy owing to an inappropriate mesh or to errors in the code, data or the mathematical model then Δt becomes very small. In such cases the time integration practically stops. Thus we can guarantee the accuracy ε for all computed shapes of the free surface.

The algorithm described works very well for all the problems considered. However, we have to mention that it is constructed for problems involving interfaces with considerable deformability. If this is not the case, the method still works but is not very efficient. The crucial point here is the predictor step (42) which is constructed for a deformable interface. In the case of stiff interfaces another formula has to be applied.

3.5. Spline filtration of truncation error at interfaces

The interface is a smooth curve but its numerical approximation is only a continuous curve. This additional information can be used to increase the efficiency of the computations.

Thus we decided to smooth down the velocity field at the interface, which will also secure the smoothness of the interface via (42) and (43) if the initial shape is smooth. Conversely, from (42) and (43) it is clear that if the functions describing the free boundary, $\mathbf{x}(t)$ and $\mathbf{x}(\hat{t})$, are C^1 then the velocity field at the interface is $[C^1]^2$ too. Thus we filtrate both components of the velocity independently employing cubic splines:[38]

$$\mathrm{Sp}(q)|_{[a_i,b_i]}=A_0+A_1q+A_2q^2+A_3q^3, \qquad \bigcup_1^n [a_i,b_i]=[a,b], \tag{52}$$

$$\mathrm{Sp}'(q)|_{a_i}=\mathrm{Sp}'(q)|_{b_{i-1}}, \qquad \mathrm{Sp}''(q)|_{a_i}=\mathrm{Sp}''(q)|_{b_{i-1}}, \qquad i=2,\ldots,n. \tag{53}$$

In our numerical examples the free surface is symmetric and the boundary conditions are derived from the symmetry. If the axis y is the line of symmetry then it yields for u

$$\mathrm{Sp}''(q)|_a=0, \qquad \mathrm{Sp}''(q)|_b=0. \tag{54}$$

For v the symmetry condition (9b) is applied directly:

$$\mathrm{Sp}(q)|_{b_{n+1}}=\mathrm{Sp}(q)|_{b_{n-1}}. \tag{55}$$

There is no convenient general theory for the choice of the parameter q. It seems natural to employ the parameterization of Γ_h generated by the parametrization of the finite element sides. Consider the part of the boundary which is an FE side $\mathbf{a}_i=[a_j, b_j]$:

$$\mathbf{a}_i: \quad \mathbf{x}_i(q_i)=\mathbf{x}_{j,j+1}+0{\cdot}5(\mathbf{x}_{j+1}-\mathbf{x}_j)q_i+0{\cdot}5(\mathbf{x}_j+\mathbf{x}_{j+1}-2\mathbf{x}_{j,j+1})q_i^2, \tag{56}$$

where the parameter $q_i\in[-1, 1]$. Let the boundary consist of n such parts, numbered so that

consecutive numbers correspond to neighbouring sides. The spline points are chosen to coincide with the FE nodes at the interface and their number is $2n+1$. The parametrizations (56) are summed directly, i.e. if $\mathbf{x}=\mathbf{x}(q)\in\mathbf{a}_i$ then

$$q(\mathbf{x})=2i-n-1+q_i(\mathbf{x}), \qquad q\in[2i-n-2,\ 2i-n]. \tag{57}$$

The values $\mathrm{Sp}(q_s)$ of the spline at the nodes $q_s=1,\ldots,2n+1$, are considered as parameters. Both components of velocity are smoothed independently. The function to be minimized reads for the u-component of velocity as

$$\Phi(\mathrm{Sp},U)=\sum_{s=1}^{2n+1} p_s(U_s-\mathrm{Sp}(q_s))^2+p\int_{-n}^{n}(\mathrm{Sp}''(q))^2\,\mathrm{d}q. \tag{58}$$

The weights p_s determine the deflection of $\mathrm{Sp}(q_s)$ from the value of the u-component of velocity at the spline nodes q_s, i.e. the deviation of the new values of velocity in the points at the free boundary from the old one. The weight p corresponds to the requirement for minimal curvature of the spline.

There is no general theory on how to choose these parameters. We employ the choice

$$p_i=1, \quad i=1,3,\ldots,2n+1, \qquad p_i=0{\cdot}85, \quad i=2,4,\ldots,2n, \qquad p=C\cdot 2n. \tag{59}$$

The parameter values p_i at a side's ends are chosen to be 20% greater than at the mid-side points because we know from numerical experiments that the solution is slightly worse at the former. The coefficient p is taken to be proportional to the length of the interval $[a, b]$ and C is chosen between 0·5 and 1·0.

It is clear that the results with and without the use of spline smoothing should coincide. We do not know an exact solution for an appropriate free boundary problem to use as a test. Thus we just solve the problem of a rising bubble in a spherical container at $Re=5$ and $Eo\equiv We/Fr=9$ studied by Shopov *et al.*[28] with and without the use of splines and compare the results in Table II.

The algorithm without spline smoothing performs during the computations the following time steps: one with $\Delta t=0{\cdot}06$, one with $\Delta t=0{\cdot}02$, 38 with $\Delta t=0{\cdot}0266$, one with $\Delta t=0{\cdot}053$, altogether 41 legitimate steps, two steps are cast down, average time step $\Delta t=0{\cdot}028$. The computations with spline smoothing proceed in the following way: three steps with $\Delta t=0{\cdot}06$, four with $\Delta t=0{\cdot}12$, two with $\Delta t=0{\cdot}08$, one with $\Delta t=0{\cdot}32$, altogether 12 legitimate steps, one cast down, average $\Delta t=0{\cdot}1$. The computer time is 3·4 times less when splines are employed.

We have done many other experiments which also confirm that the difference between the results with and without spline smoothing is within the range of error of the method. Moreover, they show that the use of splines decreases the CPU time by 20%–70%. However, this technique has to be used carefully, with small enough $\Delta t_{\max}$ and smoothing coefficient p. As usual there exists a delicate balance between the computer time used and the exactness of the results.

Table II. Comparison in the uniform norm $|\mathbf{x}|_c=|x|_c+|y|_c$ between the results with and without spline smoothing

Time	Difference $\lvert\mathbf{x}\rvert_c$	Time	Difference $\lvert\mathbf{x}\rvert_c$
0·12	$0{\cdot}234\times10^{-2}$	0·72	$0{\cdot}956\times10^{-2}$
0·18	$0{\cdot}196\times10^{-2}$	0·76	$0{\cdot}935\times10^{-2}$
0·24	$0{\cdot}250\times10^{-2}$	0·80	$0{\cdot}923\times10^{-2}$
0·35	$0{\cdot}455\times10^{-2}$	0·88	$0{\cdot}971\times10^{-2}$
0·48	$0{\cdot}659\times10^{-2}$	1·20	$0{\cdot}148\times10^{-1}$
0·60	$0{\cdot}824\times10^{-2}$		

4. NUMERICAL TESTS, COMPARISONS AND EXAMPLES

All problems under consideration are transient and the steady state (if it exists) is a limit of the unsteady one for sufficiently large time. Unless otherwise stated, the problem is assumed to be 2D axisymmetric.

4.1. Tests and comparisons

Deformation of a bubble by gravity and 'antigravity'. This is a simple model problem without direct physical meaning, which is similar to deformation of a fluid particle in a unaxial straining flow.[12] It is used to test the technique as a whole as well as the efficiency of its variants. This is a suitable test because some qualitative characteristics of the flow can be assessed is a preliminary step and the numerical results can be estimated with respect to this assessment.

We consider an initially spherical bubble submerged in a quiescent liquid, the origin of the co-ordinate system being chosen to coincide with the position of the bubble centroid in the initial moment $t=0$. It is assumed that the only external force is

$$\mathbf{F} = -\operatorname{sign}(y)\,\rho g\mathbf{e},$$

where $\mathbf{e}$ is the unit vector in the Oy-direction, ρ is the density of the liquid and g is the gravitational acceleration, i.e. the gravity force acts above the axis $y=0$ and the 'antigravity' force acts below this axis. It is evident from the mathematical formulation (see Section 2) that the stable static state of the free boundaries (if such a state exists) depends only on the ratio of Weber and Froude numbers. This fact is used to verify the approximation of the surface tension and gravity forces.

The problem is considered in a quarter of the domain because of the symmetry with respect to the Ox- and Oy-axis. The undeformed bubble radius l is chosen as a reference length and the reference velocity is $U=\mu/l\rho$. With this choice the Reynolds number is equal to one.

As mentioned before, the steady interface shapes for $We=1$, $Fr=1$, $We=2$, $Fr=2$ and $We=4$, $Fr=4$ have to coincide and indeed the numerically obtained shapes differ by 1%. The dependence of the final shapes on $Eo = We/Fr$ is illustrated in Figure 4.

In order to assess the convergence of the method, this problem is solved at $We=5$, $Fr=0{\cdot}0222$ using three different meshs $\mathscr{A}$, $\mathscr{B}$ and $\mathscr{C}$ consisting of nine, 36 and 144 elements respectively. Mesh $\mathscr{B}$ (see Figure 5) is obtained by dividing every element of mesh $\mathscr{A}$ into four parts uniformly in both directions. Mesh $\mathscr{C}$ is obtained in the same way from mesh $\mathscr{B}$.

The dependence of the distance between the bubble shapes obtained by different meshes on time is presented in Figure 6. These results are obtained in the case of comparatively large deformations of the bubble surface (see Figure 7). The distance between the shapes obtained using meshes $\mathscr{A}$ and $\mathscr{B}$, $D_{\mathscr{A}\text{-}\mathscr{B}}(t)$, is drawn with broken line, while $D_{\mathscr{B}\text{-}\mathscr{C}}(t)$ is shown by a continuous line. The $\mathscr{B}$–$\mathscr{C}$ distance is less than 0·18% from the bubble radius and is three times less than the $\mathscr{A}$–$\mathscr{B}$ one. Thus the technique shows good convergence with respect to the spatial discretization. The maximal time step $\Delta t_{\max}$ and the overall measure of the accuracy, ε, are the same in all computations, namely $\Delta t_{\max}=0{\cdot}2$ and $\varepsilon=0{\cdot}05$.

Capillary motion of a liquid in a tube. This is a simple test problem with a contact line, which has a known solution for the static weightless state.[39] Initially the tube is filled with a quiescent liquid and the free surface is horizontal (the initial contact angle is $\pi/2$). In this case we assume that the static contact angle is $\pi/4$. The capillary forces act to move the free surface to the stable position. The time evolution of the free surface is shown in Figure 8 for $Re=1$, $We=1$, $Fr=0$.

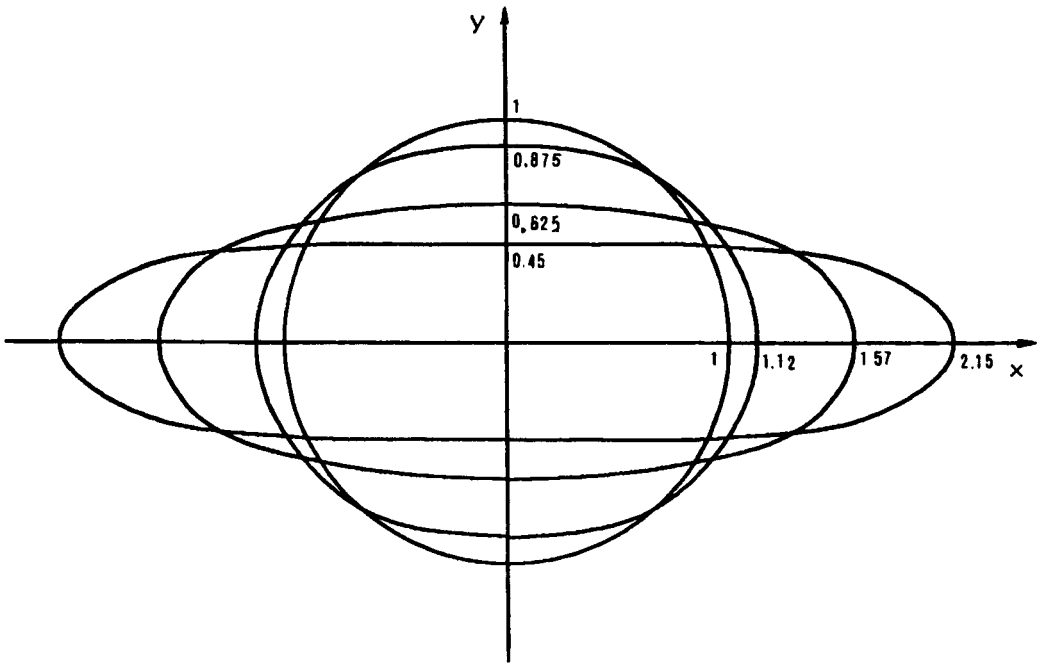

Figure 4. Bubble shapes for $Eo = 0, 1, 5, 10$

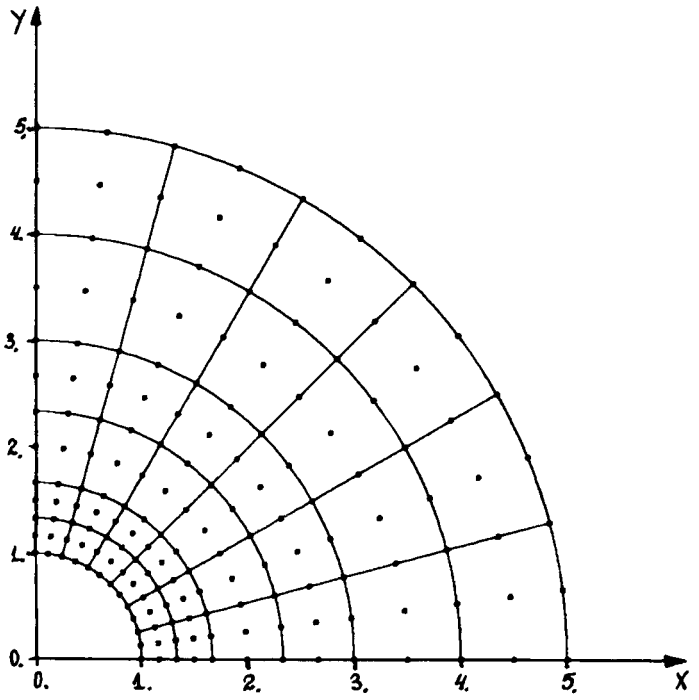

Figure 5. Initial finite element grid

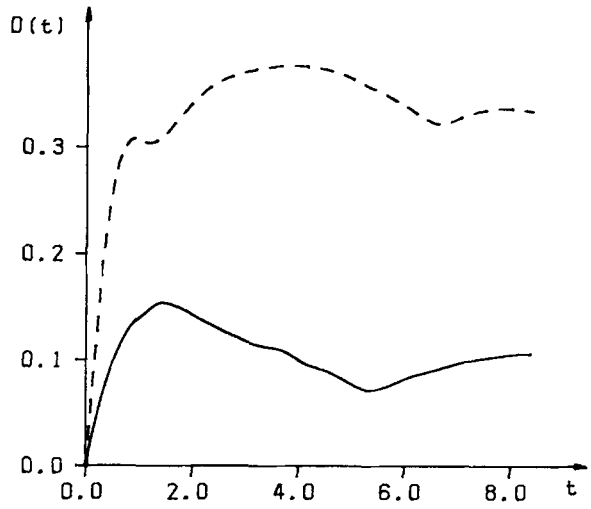

Figure 6. Graphics of $D(t)$ (%)

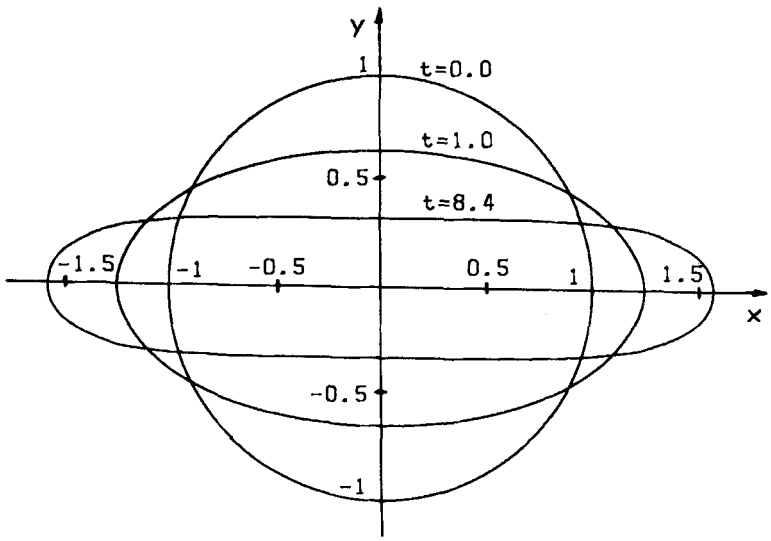

Figure 7. Time evolution of bubble shape for $We=5$, $Fr=0{\cdot}0222$

The computations are stopped when the steady state shape is reached for $t=5{\cdot}9$; at this moment the velocities in the liquid are less than 0·07%. The difference between numerical and exact solutions for the stable shape is 0·03%. The contact angle differs from the prescribed value $\pi/4$ by 0·0006 rad.

Motion of a bubble in an unbounded liquid. A complete set of comparisons between the results of Bhaga and Weber,[40] Ryskin and Leal,[10] Christov and Volkov[11] and Hnat and Buckmaster[41] for a stationary bubble rising in a viscous liquid is presented by Shopov *et al.*[28] Here we shall restrict ourselves to a comparison with the result of Bhaga and Weber.[40]

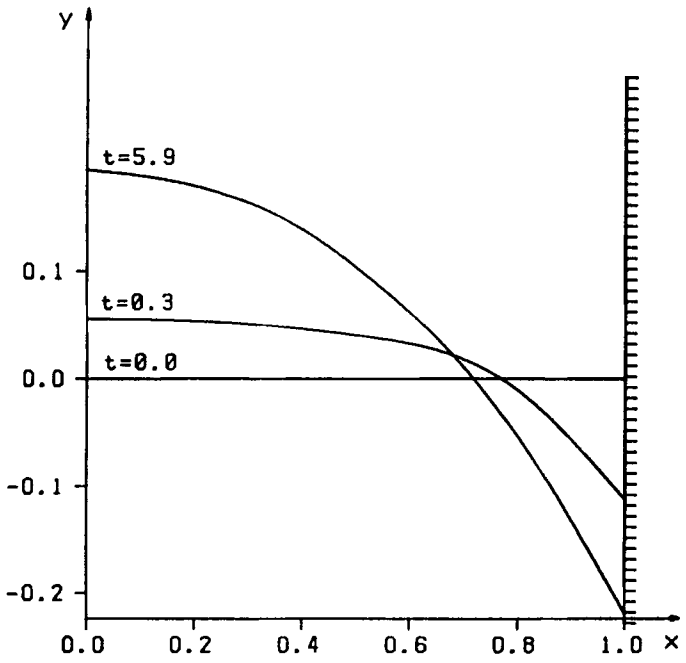

Figure 8. Position of free surface at different instants

It is well known[42] that in the limit case of zero Reynolds number the steady shape of the rising bubble is spherical for any Weber number. Bhaga and Weber[40] proved experimentally that the stable spherical shape is preserved when $Re<0{\cdot}5$ and $We<1$. In their experiment with an air bubble in aqueous sugar solution for $Re=0{\cdot}078$, $M=711$, $Eo=8{\cdot}67$ ($We=0{\cdot}055$, $Ca=0{\cdot}7$) the bubble shape is practically spherical and stable.

Our numerical experiment for the same values of the governing parameters produces a bubble shape which differs from a sphere by less than 3%. The calculations for this set of parameters are repeated on two different meshes (containing 48 and 60 elements). The difference between the steady bubble shapes obtained is less than 1%. Thus it is more appropriate to present these shapes as $r=r(\theta)$ in a polar co-ordinate system with the origin at the centroid of the bubble (see Figure 9).

An entrainment problem. An initially quiescent liquid occupying a rectangular basin is considered.[43] The right boundary impulsively starts to move upwards with unit velocity. No contact angle is specified and the liquid is assumed to adhere to the moving wall. This approach is not very natural from a physical point of view but mathematically it is well posed. The problem involves high gradients of the velocity near the wall and large deformations of the interface. The meshes at $t=0$ and $0{\cdot}51$ are presented in Figure 10. It is a severe test for our method because the elements near the moving boundary become deformed easily and the problem requires comparatively many redefinitions of meshes (about 10).

Our results and Frederiksen and Watts' results[43] for $Re=1$, $We=1$, $Fr=0{\cdot}01$ practically coincide (the graphics of the free boundary are identical at $t=0{\cdot}51$). The position of the free boundary and the velocity field are shown in Figure 11.

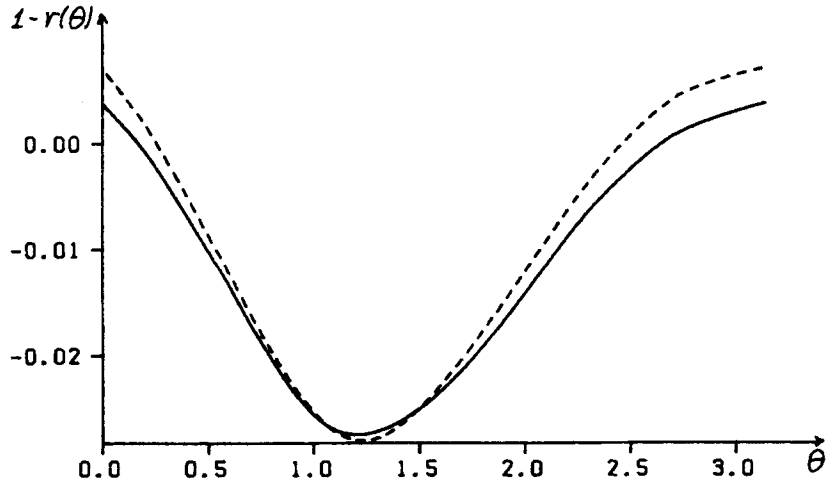

Figure 9. Graphics of $1-r(\theta)$: ---, 48-element mesh; ——, 60-element mesh

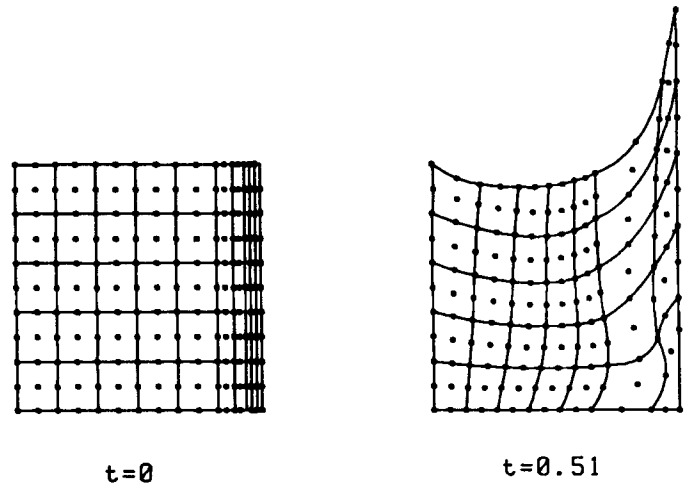

Figure 10. Initial and final finite element grids

4.2. *Numerical examples*

Motion of a bubble. The motion of a bubble due to buoyancy in an unbounded viscous liquid at relatively high Reynolds and Eötvösh numbers is considered. The volume-equivalent radius of the bubble is chosen as a characteristic length and its terminal velocity as a characteristic velocity. In this example we try to get a feeling for when the unstable regimes occur in the numerical calculations. Thus we fix the Reynolds and Eötvösh numbers and look for a stable shape. If one is reached then we increase the parameters until there is no stable state. This situation takes place at $Re=47$, $Eo=29$ in Figure 12; the first shape is the steady one at $Re=6{\cdot}65$, $Eo=29$. The experimental result of Bhaga and Weber[40] for identical parameters shows that the steady shape of the bubble is a spherical cap with a very sharp edge. In our numerical experiment the shape of the bubble is qualitatively the same for sufficiently large time. However, it is not absolutely steady. It

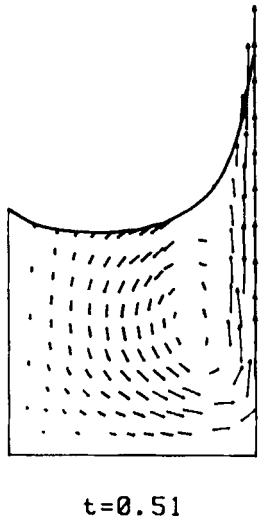

Figure 11. Numerical solution for $Re=1$, $We=1$, $Fr=0{\cdot}01$, $t=0{\cdot}51$

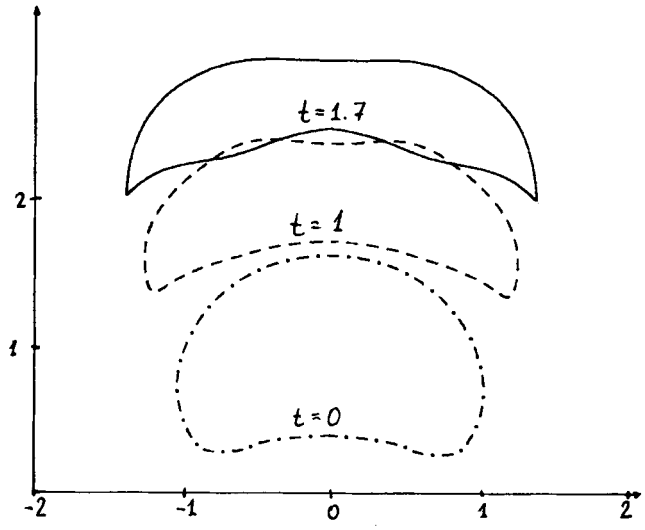

Figure 12. Numerical shapes for $Re=47$, $Eo=29$

is clear in Figure 12 that a surface wave appears initially in the front part of the bubble and then gradually moves to its rear. The experimental study[40] shows that this set of parameters is near the critical values when the free boundary and the flow lose stability and so-called skirted regimes appear.

Interaction of a bubble with a rigid wall. Another interesting problem is the interaction of a bubble which moves at its steady state regime with a rigid wall. The solution of this problem is obtained by taking a steady state solution for a bubble rising due to buoyancy in an unbounded liquid and using it for an initial condition.

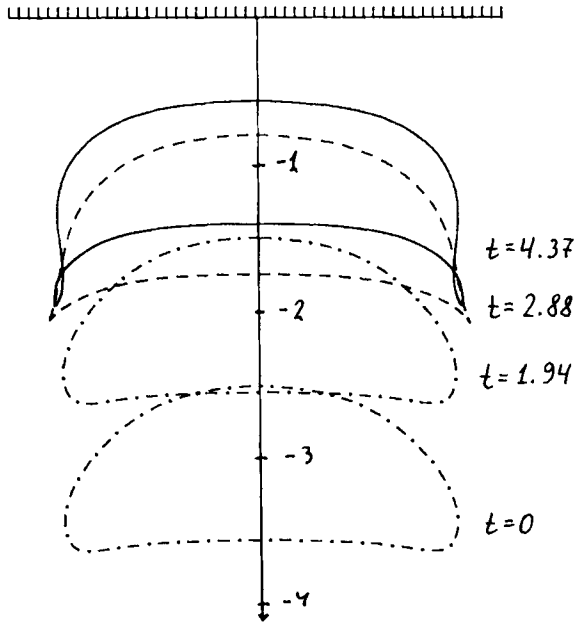

Figure 13. Motion of a bubble to a plate for $Re=19{\cdot}4$, $We=15{\cdot}3$, $Fr=0{\cdot}38$, $d=1{\cdot}5$

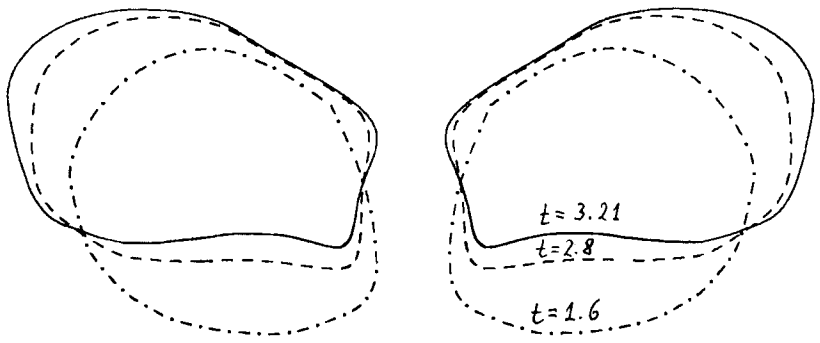

Figure 14. Hydrodynamical interaction of two bubbles and a plate for $Re=9$, $We=40$, $Fr=2$

Numerical results for an initial distance $d=1{\cdot}5$ are presented in Figure 13. An inertial concavity develops quickly. This leads to very sharp rims on the particle. Self-crossing of the liquid–gas interface takes place in the last shape presented. This is a sign that small bubbles will separate from the rim, but modelling of this stage is not done because it is outside the scope of the present technique.

Motion of two bubbles towards a rigid wall. The following problem treats the parallel motion of two bubbles towards a rigid wall. We consider the planar case, i.e. we assume that the bubbles are in a Hele–Shaw cell and can be considered as two-dimensional. The numerical example presented in Figure 14 shows the capability of the numerical technique to solve free boundary problems in a

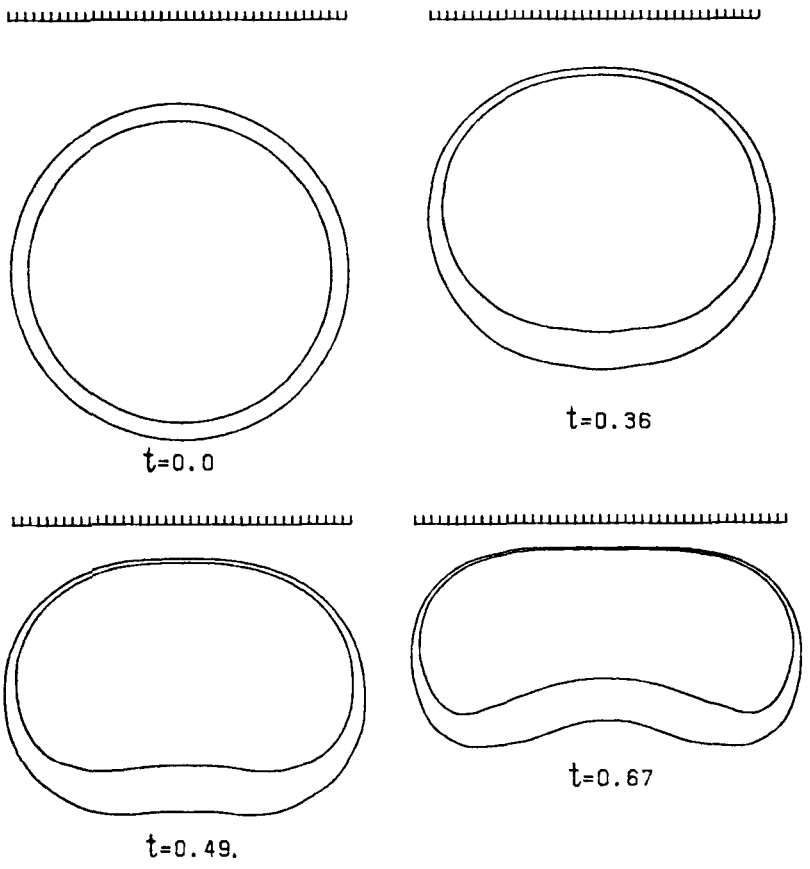

Figure 15. Motion of a compound drop to a plate for $Re=1$, $We=5$, $Fr=0{\cdot}222$, $\lambda=2$, $\eta=0{\cdot}1$ $\kappa=2$, $d=1{\cdot}5$, $e=0{\cdot}9$

multiply connected domain. As is clear from the figure, the two bubbles influence each other and as a result their shapes are not symmetrical as in the case of single particle for similar parameters.[28]

Hydrodynamical interaction of a compound drop with a plate. The motion of an A-type compound drop towards a rigid wall under gravity is considered in this example. The particle consists of a gas bubble completely covered with a layer of a liquid. Initial conditions are: perfectly symmetrical compound drop and zero velocity field. The initial distance between the centroid of the particle and the plate is $d=1{\cdot}5$.

The evolution of the interfaces at intermediate Reynolds number is presented in Figure 15. At $t=0{\cdot}67$ a double film is formed between the gas phase and the wall and an inertial concavity appears at the rear of the particle. A similar effect is observed in the study of a bubble rising towards wall.[28]

5. CONCLUSIONS

In this paper we have presented an FE method for the transient Navier–Stokes equations in domains with free boundaries. The method is of Lagrangian type and employs mesh redefinition

and a divergence-free basis. Particular attention is paid to the case of surface tension as a surface force. The method is provided with automatic time step selection, accuracy control and optional spline filtration of the velocities at the deformable interfaces. Treatment of one or several free surfaces of gas–liquid or liquid–liquid type is possible.

Comparisons with other numerical results, some steady state exact solutions and solutions on two grids are presented. They show good agreement and reliability of the method. The method works well for low and intermediate Reynolds numbers and for arbitrary deformability of the free surface, but is not so robust in the case of very low deformability. This is connected with the concrete predictor step employed, which is constructed for intermediate and large deformability. Perhaps this inefficiency could be avoided by the use of another predictor.

The described technique is tested on a number of problems with free surfaces and numerical examples related to the dynamics of bubbles or multiplde drops are included. More numerical examples can be found in Reference 28. They show that this method is a reliable and flexible tool for multiphase flows and related problems.

ACKNOWLEDGEMENTS

We thank Professor R. E. Ewing and Professor R. D. Lazarov for fruitful discussions on the topic and the manuscript and Professor Z. D. Zapryanov for encouraging us to study this subject.

This study is partially supported by Grant 100 and Grant 100-00-239 of the Bulgarian Ministry of Science and Higher Education.

REFERENCES

1. F. H. Harlow and J. E. Welch, 'Numerical calculations of time-dependent viscous incompressible flow of fluid with free surface', *Phys. Fluids*, **8**, 2182–2189 (1965).
2. C. W. Hirt, J. L. Cook and T. D. Butler, 'A Lagrangian method for calculating of incompressible fluid with free surface', *J. Comput. Phys.*, **5**, 214–222 (1970).
3. B. D. Nichols, C. W. Hirt and R. S. Hotchkiss, 'SOLA-VOF: a solution algorithm for transient fluid flow with multiple free boundaries', *Los Alamos Scientific Laboratory Report LA-8355*, August 1980.
4. F. H. Harlow and J. P. Shannon, 'The splash of a liquid drop', *J. Appl. Phys.*, **38**, 3855–3866 (1967).
5. C. W. Hirt and B. D. Nichols, 'Volume of fluid (VOF) method for the dynamics of free boundaries', *J. Comput. Phys.*, **39**, 201–226 (1981).
6. J. Fromm, 'Numerical calculation of the fluid dynamics of drop-on-demand jets', *IBM J. Res. Develop.*, **28**, 322–333 (1984).
7. V. J. Rivkind, G. M. Ryskin and G. A. Fishbein, 'Motion of a spherical drop in viscous flow', *J. Eng. Phys.*, **20**, 1023–1038 (1971) (in Russian).
8. V. J. Rivkind, 'Steady motion of deformable viscous drop', *Zap. Naucn. Sem. Leningrad. Otdel. Mat. Inst. Steklov (LOMI)*, **84**, 220–243 (1984).
9. G. M. Ryskin and L. G. Leal, 'Numerical solution of free-boundary problems in fluid mechanics, Part 1, The finite difference technique', *J. Fluid Mech.*, **148**, 1–17 (1984).
10. G. M. Ryskin and L. G. Leal, 'Numerical solution of free-boundary problems in fluid mechanics, Part 2, Buoyancy-driven motion of a gas bubble through a quiescent liquid', *J. Fluid Mech.*, **148**, 19–35 (1984).
11. C. I. Christov and P. Volkov, 'Numerical investigation of the steady viscous flow past a resting deformable bubble', *J. Fluid Mech.*, **158**, 341–364 (1984).
12. I. S. Kang and L. G. Leal, 'Numerical solution of axisymmetric, unsteady free-boundary problems at finite Reynolds number. I. Finite difference scheme and its application to the deformation of a bubble in a unaxial straining flow', *Phys. Fluids*, **30**, 1929–1940 (1987).
13. F. Shokoohi and H. G. Elrod, 'Numerical investigation of the disintegration of liquid jets', *J. Comput. Phys.*, **71**, 324–342 (1987).
14. D. S. Dandy and L. G. Leal, 'Buoyancy-driven motion of a deformable drop through a quiescent liquid at intermediate Reynolds numbers', *J. Fluid Mech.*, **208**, 161–192 (1989).
15. R. Piva, A. Di Carlo and J. Guj, 'Finite element MAC scheme in general curvilinear coordinates', *Comput. Fluids*, **8**, 225–241 (1980).
16. M. Strani and R. Piva, 'Surface tension driven flows in micro-gravity conditions', *Int. j. numer. methods fluids*, **2**, 367–386 (1982).

17. M. Strani, R. Piva and G. Graciani, 'Thermocapillary convection in a rectangular cavity: asymptotic theory and numerical simulation', *J. Fluid Mech.*, **130**, 347–376 (1983).
18. J. J. Connor and C. A. Brebbia, *Finite Element Techniques for Fluid Flow*, Newness–Butterworths, New York, 1977.
19. K. Nakajima and A. Shima, 'Analysis of the behaviour of a bubble in a viscous incompressible liquid by finite element method', *Eng.-Arch.*, **46**, 21–34 (1977).
20. P. Bach and J. Villadsen, 'Simulation of the vertical flow of a thin, wavy film using a finite-element method', *Int. J. Heat Mass Transfer*, **37**, 815–827 (1984).
21. C. Cuvelier, A. Segal and A. A. van Steenhoven, *Finite Element Methods and Navier–Stokes Equations*, Reidel, 1986.
22. N. P. Kruyt, C. Cuvelier, A. Segal and J. van Zanden, 'A total linearization method for solving viscous free boundary flow problems by the finite element method', *Int. j. numer. methods fluids*, **8**, 351–363 (1988).
23. D. R. Lynch and W. G. Gray, 'Finite element simulation of flow in deforming regions', *J. Comput. Phys.*, **36**, 135–153 (1980).
24. D. L. Lynch, 'Unified approach to simulation on deforming elements with application to phase change problems', *J. Comput. Phys.*, **47**, 387–411 (1982).
25. R. Keunings, 'An algorithm for the simulation of transient viscoelastic flows with free surface', *J. Comput. Phys.*, **62**, 199–220 (1986).
26. P. J. Shopov, 'Numerical method for nonstationary Navier–Stokes equations with free boundaries', *Proc. V Int. Symp. on Numerical Methods in Engineering Vol. 2*, Lozana, 1989, pp. 752–762 (1990).
27. P. J. Shopov, P. D. Minev and I. B. Bazhlekov, 'Grid redefinition and usage of splines in computer simulation of multiphase flows', *Proc. XIV Natl Summer School 'Numerical Methods and Applications'*, August–September 1988, Varna, Sofia, 1989, pp. 202–205 (1990).
28. P. J. Shopov, P. D. Minev, I. B. Bazhlekov and Z. D. Zapryanov, 'Hydrodynamical interaction of a deformable bubble with a rigid wall at moderate Reynolds numbers', *J. Fluid Mech.*, **201**, 241–271 (1990).
29. E. B. Dussan V, 'On the spreading of liquids on solid surfaces: static and dynamic contact lines', *Ann. Rev. Fluid Mech.*, **11**, 371–400 (1979).
30. M. S. Engelman, R. L. Sani, P. M. Gresho and M. Bercovier, 'Consistent vs. reduced integration penalty methods for incompressible media using several old and new elements', *Int. j. numer. methods fluids*, **2**, 25–42 (1982).
31. A. Fortin, M. Fortin and J. J. Gervais, 'A numerical simulation of the transition to turbulence in a two-dimensional flow', *J. Comput. Phys.*, **70**, 295–310 (1987).
32. K. A. Cliffe and D. A. Lever, 'A comparison of finite-element methods for solving flow past a sphere', *J. Comput. Phys.*, **62**, 321–330 (1986).
33. K. J. Ruschak, 'A method for incorporating free boundaries with surface tension in finite element fluid-flow simulators', *Int. j. numer. methods eng.*, **15**, 639–648 (1980).
34. P. J. Shopov, 'Condensation method for hydrodynamic problems', *Serdica*, **10**, 198–205 (1984) (in Russian).
35. P. J. Shopov, 'Isoparametric finite elements with internal condensation', *C. R. Acad. Bulg. Sci.*, **35**, 913–916 (1982) (in Russian).
36. G. K. Batchelor, *An Introduction to Fluid Dynamics*, Cambridge University Press, Cambridge, 1967.
37. D. Griffiths, 'Finite elements for incompressible flow', *Math. Methods Appl. Sci.*, **1**, 16–31 (1979).
38. S. Stechkin and B. Subbotin, *Splines in Numerical Mathematics*, Nauka, Moscow, 1976.
39. R. Finn, *Equilibrium Capillary Surfaces*, Springer, New York, 1986.
40. D. Bhaga and M. Weber, 'Bubbles in viscous liquids: shapes, wakes and velocities', *J. Fluid Mech.*, **105**, 61–85 (1981).
41. J. G. Hnat and J. D. Buckmaster, 'Spherical cap bubbles and skirt formation', *Phys. Fluids*, **19**, 182–194 (1976).
42. T. Taylor and A. Acrivos, 'On the deformation and drag of a falling viscous drop at low Reynolds number', *J. Fluid Mech.*, **18**, 466–476 (1964).
43. C. S. Frederiksen and A. M. Watts, 'Finite-element method for time-dependent incompressible free-surface flow', *J. Comput. Phys.*, **39**, 282–304 (1981).